Semi-analytical model for thermal response of anhydrite radiant slab

Abdelatif Merabtine, Abdelhamid Kheiri, Salim Mokraoui, Abderrezak Belmerabet

1 Semi-analytical model for thermal response of anhydrite radiant

2 slab

3 Abdelatif Merabtine[a,b,*], Abdelhamid Kheiri[c], Salim Mokraoui[d], Abderrezak

4 Belmerabet[b,c]

5 [a]GRESPI, Université de Reims Champagne-Ardenne, Campus Moulin de la Housse, 51687
6 Reims Cedex, France

7 [b]EPF School of Engineering, 2 rue Fernand Sastre, 10430, Rosières-Prés-Troyes, France

8 [c]Université de Lorraine, Lemta, CNRS, Nancy. France

9 [d]College of Engineering, Chemical Engineering Department, King Saud University Riyadh,
10 Saudi Arabia

11 *E-mail address: abdelatif.merabtine@epf.fr; Phone number: +(33) 618 711 484

12 Abstract

13 The choice of heating systems in buildings is primarily guided by the desired comfort level

14 and energy saving concerns. Radiant floor heating systems are suitable for satisfying these

15 requirements by considering the trade-off between minimizing the thermal inertia of the

16 radiant slab and maintaining the surface temperature below a certain value. In this study, a

17 new simplified model based on an analytical correlation is proposed to evaluate the heating

18 radiant slab surface temperature and examine its thermal behavior under dynamic conditions.

19 A full-scale test cell, monitored by a set of sensors, was used to obtain measurements under

20 transient conditions. In addition, numerical models based on the finite difference method and

21 the finite volume method were developed and validated under transient conditions. The design

22 of experiments method is used to derive meta-models for the time constant and the delay time

23 in order to compute the surface temperature. The sensitivity analysis indicated that the

24 specific heat capacity of the slab material and the heating water flowrate significantly affect

25 the time constant as opposed to the insignificant effect of the thermal conductivity and the

26 heating water pipe inner diameter. In addition, it was found that all of these parameters,

27 except for the heating water flowrate, have a significant impact on the delay time. Compared

28 to the experimental results, the maximum relative deviations on the computed surface

29 temperature were within 2% for the numerical model and 4% for the semi-analytical model.

30 **Keywords:** floor heating system, experimental test cell, semi-analytical model, finite

31 difference method, finite volume method, design of experiments

32 **Nomenclature**

A_i	Surface area of wall "i" [m²]
A_s	Surface area of the FHS [m²]
$C_{p,f}$	Specific heat of the water [J·kg^{-1}·K^{-1}]
C_p	Specific heat of the anhydrite slab [J·kg^{-1}·K^{-1}]
$C_{p,a}$	Specific heat of the ambient air [J·kg^{-1}·K^{-1}]
D_0	Pipe outer diameter [m]
D_i	Pipe inner diameter [m]
e	Thickness of anhydrite slab [m]
Gr	Grashof number
h	Total convective heat transfer coefficient [W·m^{-2}·K^{-1}]
h_c	Air convective heat transfer coefficient [W·m^{-2}·K^{-1}]
h_f	Water convective heat transfer coefficient [W·m^{-2}·K^{-1}]
h_r	Radiative heat transfer coefficient [W·m^{-2}·K^{-1}]
L	Length of radiant slab (x-direction) [m]
l	Distance between pipes [m]
$\dot{m}_f$	Water mass flow rate [kg.s^{-1}]
Nu	Mean Nusselt number for air
Nu_f	Mean Nusselt number for water
Pr	Prandtl number, $Pr = \frac{\rho_f v c_f}{\lambda_f}$
Ra	Rayleigh number, $\frac{g\beta}{v\alpha}(T_s - T_a)L^3{}_c$
Re	Reynolds number, $Re = \frac{\dot{V} d}{v A_p}$
R_a	Total thermal equivalent resistance [K·W^{-1}]
R_{conv}	Thermal resistance regarding the convective heat transfer [K·W^{-1}]
R_{rad}	Thermal resistance regarding the radiative heat transfer [K·W^{-1}]
R_{cond}	Thermal resistance regarding the conductive heat transfer [K·W^{-1}]
R_p	Thermal resistance of the pipe [K·W^{-1}]
S	Pipe cross-sectional area [m²]
T_s	Surface temperature of radiant slab [°C]

$T_{s,0}$	Surface temperature of radiant slab at $t = 0$ [°C]
$T_{s,\infty}$	Surface temperature of radiant slab at the steady state [°C]
T_d	Depth temperature of the radiant slab [°C]
T_a	Ambient air temperature [°C]
$T_{a,i}$	Ambient air temperature at $x = 0$ [°C]
$T_{a,o}$	Ambient air temperature at $x = L$ [°C]
T_{rad}	Radiant temperature [°C]
T_{pi}	Inner surface temperature of the tube [°C]
T_{po}	Outer surface temperature of the tube [°C]
$T_{f,i}$	Inlet water temperature [°C]
$T_{f,o}$	Outlet water temperature [°C]
$\overline{T_f}$	Average water temperature [°C]
$\overline{T_s}$	Average Surface temperature of radiant slab [°C]
t_d	Delay time [s]

Greek letters

ε	Radiative emissivity of radiant slab [-]
λ_a	Air thermal conductivity [W·m⁻¹·K⁻¹]
λ_c	Thermal conductivity of anhydrite slab [W·m⁻¹·K⁻¹]
λ_f	Water thermal conductivity [W·m⁻¹·K⁻¹]
λp	Thermal conductivity of pipe [W·m⁻¹·K⁻¹]
ρ	Density of the anhydrite slab [kg·m⁻³]
ρ_a	Density of the ambient air [kg·m⁻³]
ρ_f	Water density [kg·m⁻³]
σ	Stefan-Boltzmann constant = 5.67×10^{-8} [W·K⁻⁴]
$\overline{\tau}$	Average time constant [s]
Φ	Total heat flux [W]
Φ_{conv_f}	Convective heat flux between the water and the inside tube surface [W]
Φ_{tube}	Conductive heat flux between the inside and the outside tube surfaces [W]
Φ_{cond}	Conductive heat flux of the radiant slab [W]
Φ_{conv_a}	Convective heat flux between the slab surface and the ambient air [W]
Φ_{rad}	Radiative heat flux between the slab surface and the surroundings [W]

1. Introduction

33

34   The building sector is currently experiencing a significant increase in the use of floor

35   heating systems (FHS). The FHS technology has become simpler because of the use of cross-

36   linked polyethylene PEX-tubes. In addition, these systems offer optimal thermal comfort and

37   improved living conditions for the occupants compared to conventional systems [1,2].

38   However, for design and control purposes, a special emphasis had to be placed on the heating-

39   slab surface temperature and the heat flowrate [3].

40   Lightweight or heavy radiant slabs perform differently because of the thermal inertia

41   characteristics of the slab material. In the lightweight systems, aluminum panels with bottom

42   insulation are typically used, which ensures a homogeneous surface temperature distribution.

43   They are also characterized by a rapid thermal response, lower heat losses, and less floor load

44   because of their low mass [4]. Heavy systems are primarily constructed with concrete or

45   anhydrite materials integrated with embedded pipes. The drawback of heavy radiant slabs is

46   their low thermal response, particularly for intermittently occupied rooms [5]. However,

47   heavy systems can be used as "thermal batteries", as the thermal energy is stored by the mass

48   concrete slab and radiated to the indoor environment with a time delay. Using heavy heated

49   floors in covered structures under controlled internal air temperature conditions can moderate

50   the heating demand [6-8].

51   In all cases, irrespective of the type of FHS and the climatic and building dynamic

52   conditions, the heating slab surface temperature must be maintained below a maximum value,

53   i.e., 28 °C/29 °C, as specified by the European committee for standardization [9], and in the

54   same time, the surface heat rate provided by the slab needs to satisfy the heating power

55   requirement of the building.

56   The FHS thermal behavior has been an ongoing research topic for a number of years [10-

57   19]. Various analytical, numerical, and simplified-model approaches have been used for this

58   purpose. Analytical models were developed by a number of authors [18-22] using a detailed

59   mathematical description of the heat transfer process. The aim of these models was to derive

60   the critical parameters, namely the radiant slab surface temperature and total heat rate. In

61 these approaches, the heat transfer equations in the slab are solved using the separation of

62 variables method, the Fourier decomposition method, or the Laplace transformation method.

63 However, the analytical approach is less used because of the complexity of solving two-

64 dimensional (2D) and three-dimensional (3D) heat transfer problems under transient

65 conditions.

66 Following the development of fast and high-capacity computers, numerical approaches

67 have become the primary tool to achieve detailed and accurate multi-dimensional thermal

68 analyses of heating slabs. Finite difference, finite volume, or finite element methods are the

69 typical classical robust techniques to solve transient heat transfer problems. Numerous authors

70 have used a numerical approach to obtain discrete thermal responses in steady- and unsteady-

71 state conditions for heating slabs [12, 17, 21]. Despite their relative accuracy, the numerical

72 simulations require significant computation time, therefore, they are not compatible with

73 quick engineering designing of heating slabs, specifically when optimization of the thermal

74 behavior of the building envelope and heating devices under actual external climatic

75 conditions are required.

76 Simplified models are based on simple energy balance or on the analysis of the thermal

77 resistances and capacitance of slab layers [22-26]. These models are useful, simple to build,

78 can offer significant flexibility for design and control purposes, and can also be combined

79 with other numerical models. They require less computation time and could provide a level of

80 accuracy comparable to the analytical or numerical models. Jin et al. [22] developed a

81 numerical correlation for the thermal conductivity of the embedded-pipe floor layer and used

82 it in the proposed surface temperature calculation model. The steady-state results obtained

83 were in good agreement with their experimental data and numerical simulations. Zhang et al.

84 [23] reported a simplified method to solve the heat conduction problem of the concrete slab

85 by considering the thermal capacity and the uniformity of the radiant surface temperature. The

86 results were in good agreement with the measurements and the numerical simulations. They

87 also reported that the thermal conductivity and thickness of each layer constituting the slab

88 had a significant impact on the performance of the radiant slab. Tian et al. [24] performed a

89 numerical and analytical modelling combined with a lumped parameter method (RC) based

90 on the concept of the core temperature layer and under six different unsteady-state conditions.

91 The RC model exhibited a good agreement with the experimental and numerical results. Li et

92 al. [25] reported a simplified thermal calculation method adapted to a multilayer floor

93 structure. This method was based on the analytical solution of the Fourier law and on the

94 thermal resistance of the floor layers. They also reported an equivalent thermal resistance

95 concept to evaluate the floor surface temperature distribution. Wu et al. [26] reported a novel

96 simplified model using the conduction shape factor under steady-state conditions. The effects

97 of pipe spacing, slab layer thickness, and average water temperature on the derived surface

98 temperature and heat flux were analyzed. The obtained results indicated that the screed

99 thickness has no impact on the surface temperature as opposed to the pipe spacing and

100 average water temperature.

101   From previous studies, simplified models appear more favorable than analytical or

102 numerical approaches as they allow for a quicker evaluation of the thermal behavior of the

103 FHS, which can help to establish optimal design parameters in the early stages of the heating

104 system design. However, further aspects should be considered for complete thermal

105 characterization of the FHS radiant slab: (i) the thermal behavior of the radiant slab should be

106 studied under transient conditions in order to consider the alternating conditions between day

107 and night and abrupt variations in surroundings, such as an unscheduled overcrowd, or an

108 unexpected direct solar heating of the slab surface ; (ii) a parametric study of the radiant slab

109 thermal performance must be performed considering the simultaneous interactions of the

110 design and the thermo-physical properties. Therefore, a full sensitivity analysis exploring the

111 impact of each single parameter, as well as their simultaneous interactions, had to be

112 performed in order to determine the optimal thermal response of the FHS. To date, it appears

113 that there are few published studies that analyze the thermal dynamic behavior of the slab

114 with a practical and simple model.

115 The aim of this study is to contribute to the existing state-of-the-art by providing a valid

116 and simplified calculation model of the heating anhydrite slab thermal behavior considering

117 all primary design parameters. The design of experiments (DoE) method is used in

118 conjunction with the experimental data obtained for the floor heating surface temperature and

119 a 2D finite difference model is developed and validated. The obtained results would be of

120 significant practical use for building engineers and designers, and allow accurate thermal

121 behavior predictions of the FHS for design or control purposes.

122 In the second section, the monitored full-scale experimental test cell incorporating the

123 FHS is discussed. The 2D finite difference model (FDM), which was developed by Merabtine

124 et al. [6], is then improved and adapted for our case study. In addition, a 3D numerical model

125 of the FHS based on the finite volume method (FVM) is presented and validated under

126 transient conditions. A simplified analytical model with time constant and delay time for the

127 average floor heating surface temperature is then proposed. A multi-objective sensitivity

128 analysis based on the DoE method is then performed to analyze the effects of the design

129 parameters and physical properties of the FHS on the time constant and the delay time,

130 yielding unique meta-models. These meta-models represent the correlations that relate the

131 time constant and the delay time to the different design and physical parameters.

132 Subsequently, the complete simplified model equation is obtained and validated using the

133 meta-models as its coefficients. The proposed methodology is shown in Figure 1.

134

135   Figure 1: Schematic diagram of proposed methodology

136

2. Experimental section

2.1. Overview of the test cell facility

The experimental facility is a full-scale test cell (Fig. 2a) that is designed with a dual purpose allowing both the study of the characterization of the building envelope materials and the thermal comfort assessment. The 2.1-m-high test-cell envelope is a wooden structure with a total heated area of 11 m² and insulation made from hemp wool and wood fibers. These materials were selected for their good thermal insulation properties and considering the French building standards. Figure 2b shows the test cell dimensions, as well as the envelope material types and the location of the sensors. The test cell comprises two controlled and monitored hygrothermal zones: the inside test zone, which simulates the indoor environment, and the outside zone, which simulates a number of outdoor conditions. The rooms are separated by a partition with an opening to accommodate building materials to study their hygrothermal behavior when subjected to different climatic conditions. The behavior of the envelope materials is not addressed in this study. This partition is considered as an exterior facade and not as an interior wall. Therefore, it is subjected to a warm atmosphere on the left-hand side and an air-conditioned atmosphere on the right-hand side.

(a)

(b)

Figure 2: Experimental test cell: (a) outside view, and (b) plane view

As shown schematically in Figure 3, the test cell is equipped with a number of heating, ventilation, and air conditioning (HVAC) systems connected to a regulator allowing complete

161 control of both indoor and outdoor conditions. The heating of the indoor environment is by

162 means of a heat pump (1) supplying three distinct heat emission systems (4, 5, and 6). The

163 heat pump provides the required heat to the water that flows in the system. The buffer tank (2)

164 installed between the heat pump and the circulation pumps (3) provides additional water

165 storage in the heating system to prevent boiler short cycling. The first circuit supplies the

166 radiant slab (6), the second one supplies the radiators (5), and the third one supplies the

167 convective radiator referred to as the variable air volume (VAV) (4). Each circuit is equipped

168 with its own circulation pump to ensure the chosen temperature and volume flow rate of the

169 hot water. A three-way valve and a thermostatic valve are put to control the water

170 temperature at the inlet of the radiant slab. An ambient thermostat monitors the room

171 temperature and controls the heat pump. The outside zone is cooled by an air conditioning

172 system (7). The HVAC systems characteristics are presented in Table 1.

173 **2.2. Experimental procedure**

174   In order to validate our proposed numerical models, regardless of the input conditions,

175 two scenarios were experimentally simulated in this study. In the first scenario, the inlet water

176 temperature was adjusted in two successive levels , at 27.5 and 29 °C, during pre-defined

177 times (Table 1). In the second scenario, the inlet water temperature was kept constant at 31.5

178 °C..

179

180

181   Figure 3: HVAC systems

182

183 Table 1: Test cell facility overview

184

185   The measured data was recorded at five-minute intervals by an acquisition system and

186 could be visualized over extended periods. The measured parameters are the average air

187   temperature T_a and the relative humidity (RH) of each room, the mean radiant temperature

188   T_{rad}^{meas}, the inlet and outlet water temperatures $T_{f,i}$ and $T_{f,o}$, respectively, the surface

189   temperatures T_{s1} and T_{s2}, the depth temperatures T_{d1} and T_{d2} of the floor heating radiant slab,

190   and the emitted heat flux rate ϕ of the FHS. Table 2 depicts the measuring instruments as well

191   as its measuring range and accuracy.

192

193   Table 2: Measuring instruments

194

195   The air temperature and RH of the inside zone were measured by two different sensors,

196   located at 1.8 m and 1.5 m from the floor, which were fixed in the center of the wall and in

197   the geometric center of the room. The main reason of fixing one of the two sensors into the

198   wall allows checking if there is any substantial gap between measurements due to the natural

199   convection. The air temperature and RH of the outside zone were measured by one sensor

200   located at 1.8 m from the floor and fixed to the wall. The surface temperatures of the floor

201   heating radiant slab, T_{s1} and T_{s2} were measured by two sensors. The heat flux meter was

202   placed as close as possible to the surface temperature sensors. The depth temperature sensors,

203   T_{d1} and T_{d2}, were embedded inside the screed, and were placed at 2.6 cm and 3.6 cm from the

204   insulation panel, respectively. It must be noted that, regarding the validation process, we

205   averaged all of the above measured temperatures, namely T_a, T_s, and T_d. The floor heating

206   radiant slab dimensions and the sensor locations are shown in Figure 4.

207

208   Figure 4: Sensor locations and slab dimensions: (a) cross-sectional view, and (b) top view

209

210   **3. Numerical modelling**

211   **3.1. 2D Finite difference method**

212   In a previous study [6], a 2D FDM model was developed and experimentally validated to

213   estimate the radiant floor surface temperature and the heat flowrate under transient conditions

214   in the case of a reduced scale and non-covered FHS. In this study, we aim to improve on the

215   model by making the required modifications to adapt it to a full-scale covered test cell. Once

216   validated, this model could serve as an accurate and fast numerical tool for heating floor

217   design purposes and sensitivity analyses.

218   The model of Merabtine et al. [6] included a number of assumptions, essentially similar to

219   the assumptions in other previous studies [12,14,27]:

220   i.   The slab material is homogeneous and the property parameters are kept constant

221   ii.   The pipe-wall thermal resistance is neglected

222   iii.   The floor is thermally insulated all around (bottom and vertical sides)

223   iv.   The heat transfer in the pipe (water region) is one-dimensional (radial heat transfer)

224   v.   The heat transfer in the slab is transient and 2D

225   The last assumption will be further discussed in our case study. The first natural direction

226   through which the heat flows is vertically from the pipe to the radiant surface, namely, the y-

227   axis. The other dimensions are the lengthwise, x, and widthwise, z, . These lasts will later be

228   combined in one direction, the x-axis, by assuming that the slab contains only one straight

229   pipe. In fact, the coil-shaped pipe, with a total length L, is theoretically unrolled to yield a

230   long slab of the same length L heated with a straight pipe. Therefore, the FDM model applied

231   to this physical domain is developed to provide both in-depth and surface floor temperatures

232   for the region above the pipe. A full description of the physical domain and the developed

233   numerical model is provided by Merabtine et al. [6].

234   In this study, a number of modifications of the model are made to consider the variations

235   with time of a number of parameters. In addition, the measured inlet water temperature and air

236   temperature of the inside zone were implemented in the model. The total heat transfer

237   coefficient $h(t)$ between the radiant slab surface and both the ambient air and the

238   surroundings can be estimated by summing up the convective and the radiative coefficients

239     $h_c(t)$ and $h_r(t)$. $h_c(t)$ is calculated using a correlation of the transient Nusselt number $Nu(t)$

240   for a turbulent flow which is given by [28].

241     $Nu(t) = 0.14 * Ra(t)^{0.33}$ (1)

242   where $Ra(t) = Gr(t) * Pr$, where $Gr(t) = \frac{g*L^3*\beta*([T_s(t)-T_a(t)]}{\nu^2}$, and $Pr = \frac{\mu*c_p}{\lambda_a}$

243   Once $Nu(t)$ is calculated, $h_c(t)$ is estimated as follows [28]:

244     $h_c(t) = Nu(t) * \frac{\lambda_a}{L}$ (2)

245   The calculation process is repeated for each time step to obtain $h_c(t)$ as a function of time

246   to be implemented in the 2D FDM model.

247   The value of $h_r(t)$ between the floor surface and the surrounding environment is given

248   by:

249     $h_r(t) = \varepsilon \, \sigma \, (T_s(t) + T_{rad}(t)) (T_s(t)^2 + T_{rad}(t)^2)$

250   (3)

251   The mean radiant temperature sensor, which is installed in the inside test zone, displays a

252   temperature T_{rad}^{meas} that includes the influence of all surrounding surfaces A_i, with i runs from

253   1 to n, including the floor heating surface. The value of T_{rad} is calculated by subtracting this

254   floor heating surface radiative contribution as follows:

255     $T_{rad} = \frac{B \sum_i^n A_i}{C}$ (4)

256   where $B = T_{rad}^{meas} - \left(\frac{T_s(t)A_s}{\sum_i^n A_i}\right)$,

257   and $C = (\sum_i^n A_i) - A_s$

258   where T_{rad}^{meas} is defined as:

259      $T_{rad}^{meas}(t) = \frac{\sum_i^n T_i(t)*A_i}{\sum_i^n A_i}$ (5)

260

261   As can be seen in Figure 5, the measured radiant temperature T_{rad} and the air temperature

262 of the inside zone T_a are approximately similar. Therefore, we can substitute $T_{rad}(t)$ in

263 equation (3) with $T_a(t)$. It should be noted that this similarity is not valid for all case studies

264 since this depends mainly on the outdoor temperature, the thermal insulation and the room

265 size.

266

267   Figure 5: Air ambient and radiant temperature profiles in inside zone

268   **3.2. 3D Finite volume method (FVM)**

269   The 3D FVM model was developed using computational fluid dynamics software to

270 consider the thermal losses through the z-axis. The floor heating geometry was represented by

271 a parallelepiped crossed by a tube representing the hydraulic coil. The floor dimensions

272 correspond to the actual dimensions of the heating floor.

273   The general equations governing the thermal and dynamic response of the fluid and solid

274 parts in the simulated model are as follows:

275           $\frac{\partial \rho}{\partial t} + \nabla \cdot (\rho \vec{v}) = 0$ (6)

276           $\frac{\partial}{\partial t}(\rho \vec{v}) + \nabla \cdot (\rho \vec{v} \vec{v}) = -\nabla p + \rho \vec{g}$ (7)

277           $\frac{\partial}{\partial t}(\rho h) + \nabla \cdot (\vec{v} \rho h) = \nabla \cdot (k \nabla T)$ (8)

278   The boundary conditions were chosen to match, as far as possible, the actual configuration

279 while adhering to the following assumptions:

280   i.   The underside in contact with the insulation panel and the four side faces is considered

281   adiabatic.

282   ii.   The inlet hot water is subjected to the experimental temperature implemented in the

283   3D FVM model via a User Defined Function (UDF) implemented in the used CFD

284   software. The UDF is a subroutine implemented in the FVM model that contains a

285   customized data in a matrix form to fit with the measurements.

286   iii.   The upper surface of the anhydrite radiant slab is subjected to convection with the

287   ambient air and the radiation with the surroundings.

288   iv.   The measured air temperature of the inside test zone was implemented as a UDF in the

289   3D FVM model.

290   As the meshing level has a significant impact on the accuracy of the numerical simulation

291 and the CPU time, it is essential to identify the optimal meshing in terms of the generated

292 mesh number and the computing time. For this reason, we conducted three simulations with

293 successive increase in the refined mesh refining and compared them in terms of the thermal

294 response of the FHS. Table 3 presents, for each mesh level, the simulated average surface

295 temperature at steady state together with the required number of nodes and the corresponding

296 CPU time.

297

298 Table 3: Comparison between three mesh levels

299

300   It can be seen that mesh #2 is the most optimal level regarding a trade-off between the

301 accuracy of the results and the CPU time. Therefore, this mesh level, as shown in Figure 6,

302 has been adopted in this study.

303

304

305

306   Figure 6: Domain meshing

307

4. Results and discussion

4.1. Validation of improved 2D FDM model

As mentioned in Section 3.1, the 2D FDM model in [6] was validated for the case of a radiant slab operating in an open space where the indoor room temperature variations were not considered in the model. The validation was done by comparing the calculated hot water outlet temperature, the average radiant slab surface temperature, the average heat flow, and the in-depth slab temperature at different locations to the experimental results. The model exhibited satisfactory performance; however, there remained scope to improve the performance. In the present study, the FDM model is improved by incorporating the actual measured values of the hot water inlet and the indoor air temperatures into the model. The heat transfer coefficient to the ambient air and surroundings is also modified by considering the radiative part, as discussed in Section 3.2.

In order to validate the improved 2D FDM model, we first compared the numerical simulations with those of Merabtine et al. [6] and with the experiments conducted in the test facility therein reported. As can be seen in Figure 7, the improved 2D FDM model is in good agreement with the experimental data regarding the average surface temperature, with a maximum relative error of 1%.

Figure 7: Average surface temperature profile (comparison with Merabtine et al. [6])

In the next step, the improved model is validated by comparing the numerical simulations with the measurements performed in the full-scale covered test cell with regard to the two scenarios discussed in Section 3.

4.2. Validation of 2D FDM and 3D FVM models for scenario #1

332   In order to maintain the maximum average surface temperature at 28–29 °C according to

333   the French standard NF DTU 65.14 P1-1 [29] and the European committee for standardization

334   CEN [9], the heat pump was set to supply the inlet hot water at a maximum of 35 °C. The

335   entire system was controlled by a regulating system to meet the requirements of scenario #1,

336   which has two temperature levels (27.5 °C and 29 °C ±1 °C). The 2D FDM model considers

337   the measured inlet hot water temperature, while the 3D FVM model approaches it by a curve

338   fit as it uses an UDF. The measurements were repeated three times under identical

339   experimental conditions. Figure 8 compares the experimental and the simulated average

340   surface temperature profiles.

341

342   Figure 8: Average surface temperature profiles for scenario #1

343

344   The simulation results remained within the range of the error bars and are in good

345   agreement with the experimental data, with a maximum relative error of 1.6% for both

346   models. For this scenario, the temperature takes ~38.5 h to reach the steady state, which

347   means that the thermal inertia significantly impacts the radiant slab thermal response and must

348   be carefully analyzed.

349   **4.3. Validation of 2D FDM and 3D FVM models for scenario #2**

350   In this scenario, we used the same thermo-physical and dimensional parameters as for

351   scenario #1. However, the inlet water temperature was experimentally and numerically kept

352   constant at 31.5 °C ±1 °C as the regulating system takes a certain amount of time to maintain

353   the heated water at the required temperature. Figure 9 compares the experimental average

354   surface temperature with the numerical results. The measurements were repeated three times.

355   As can be seen, the temperature profile follows a quasi-logarithmic curve with a small delay

356   time t_d that is estimated as 9 min, which is because of the regulator and the thermal inertia of

357   the slab. The transient surface temperature evolves with a time constant τ. The latter

358   characterizes the thermal inertia of the materials used in the hydraulic tube and in the screed.

359   The average surface temperature attained a steady state at ~30 °C within 15 h.

360

361   Figure 9: Average surface temperature profile for scenario #2

362

363   The estimates of the average surface temperature by the 2D and the 3D numerical models

364   were satisfactory, and there was a good agreement with the measurements with maximum

365   relative errors of ±2% and ±2.5% for the 2D FDM and 3D FVM models, respectively. The

366   errors could be related to the fact that the inlet water temperature implemented in the 3D

367   FVM model was kept constant. In addition, the sidewalls and the bottom surface of the

368   heating floor were considered adiabatic.

369   Once both numerical models were validated for the average surface temperature, other

370   simulations were conducted to estimate the temperature profile inside the radiant slab so as to

371   analyze the floor heating temperature gradient. Figure 10 compares the experimental and the

372   numerical estimated temperatures for different sensor locations at the steady- and unsteady-

373   states. The following parameters were compared: temperatures inside the screed T_{d1} and T_{d2},

374   which correspond to a height of 2.6 cm and 3.6 cm from the water pipes, respectively; the

375   average surface temperature of the anhydrite radiant slab, and the ambient air temperature that

376   corresponds to a height of 150 cm. Notice that the ambient air temperature was used in both

377   models as input data, as the numerical models were only developed for the floor heating

378   system and excluded the surrounding environment.

379

380   Figure 10: Floor heating temperature gradient from water pipes to ceiling (scenario #2)

381

382   With regard to T_{d1} and T_{d2}, the 2D model correctly estimates the temperature profile with

383   a maximum relative error of 3%. The 3D simulation results differ from the measured values

384   with a maximum relative error of 8% under the transient state. The reason for this error could

385   be because the inlet hot water temperature differed marginally from the beginning of the

386   heating at t = 0 min until t = 100 min, and this would affect the transient phase.

387   In addition, for the same water inlet conditions, the simulated and measured emitted heat

388   fluxes, which are expressed as the sum of the convection and radiation heat fluxes, are shown

389   in Fig. 11. The radiative heat flowrate (not presented here) is more critical (~2/3 of the total

390   heat flux) than the convective heat flowrate (~1/3).

391

392   Figure 11: Heat flowrate profile (scenario #2)

393

394   Regarding the radiant slab surface temperature distribution, figure 12 shows similarities

395   between the infrared thermal imaging and the simulated surface temperature field with the 3D

396   FVM model at t = 30 min. It is noteworthy that, in the 3D model, the shape of the water pipe

397   was approached by a regular shape (as compared to the actual one) in order to make easy the

398   manner of drawing on the CFD software. In the other hand, we sought to keep identical tube

399   length and the same general pattern (coil) as for the actual configuration.

400   (a)   (b)

401   Figure 12: Surface temperature distribution at t = 30 min (same temperature scale): (a)

402   numerical simulation, and (b) infrared thermal imaging (scenario #2)

403

5. Transient simplified semi-analytical modelling

5.1. Semi-analytical modelling

406   One of the significant results of the study by Pierson and Padet [30] was that the water

407   temperature evolving in a heat exchangers (HEX) has a logarithmic profile. Therefore, they

408   proposed a transient simplified formula which could be universally used for a HEX that

409   characterizes its thermal behavior. The theoretical end experimental studies conducted by

410   Pierson and Padet, show that the inlet and outlet temperatures of two water streams, a cold

411   one and a hot one, evolving in a heat exchanger in transient conditions fulfills a logarithmic

412   profile before reaching steady state conditions. As a heat exchanger, the FHS is considered as

413   a water-based system that exchanges heat from water to ambient air and the surroundings with

414   a quasi-logarithmic thermal response. Therefore, its transient thermal behavior can be studied

415   using the Pierson and Padet approach [30].

416   While this semi-analytical approach is applied to the FHS, variations in the surface

417   temperature is a time function that includes a time constant and a delay time that could be

418   estimated experimentally. This function is expressed as follows:

419
$$T_s(t) = \begin{cases} T_{s,0} & t < t_d \\ T_{s,\infty} + \left(T_{s,0} - T_{s,\infty}\right)e^{-\frac{(t-t_d)}{\tau}} & t \geq t_d \end{cases} \tag{9}$$

420   where $T_{s,0}$ is the average surface temperature at t = 0; $T_{s,\infty}$ is the average surface temperature

421   at the steady state; τ is the time constant; and t_d is the delay time. The values of τ and t_d will

422   be determined using the DoE method based on the validated 2D FDM numerical model.

423   To derive the surface steady-state temperature $T_{s,\infty}$, we can consider the entire heat

424   exchange between the hot water and the ambient air in the inside zone. The calculations are

425   performed by Equations 10–18.

426   The thermal convection between the water and the inside surface of the pipe is given by:

427    $\Phi_{Conv\_f} = h_f \pi D_i L \left(T_f - T_{pi}\right)$ (10)

428   where L and D_i are the tube length and inner tube diameter, respectively; T_f, T_{pi} are the hot

429   water bulk temperature and the inner surface temperature of the tube, respectively; and

430     $h_f = \frac{Nu_f \lambda_f}{D_i}$ is the heat transfer coefficient which can be obtained from the dimensionless

431   Nusselt number Nu_f based on the Dittus–Boelter correlation [19]:

432     $Nu_f = 0.023 Re^{0.8} Pr^{0.4}$ for $0.7 < Pr < 100$ and $Re > 10^4$ (11)

433   The thermal conduction between the inner and the outer surfaces of the tube at the steady-

434   state is expressed as:

435     $\Phi_{tube} = \frac{(T_{po} - T_{pi})}{R_p}$ (12)

436   where $R_p = \frac{ln\left(\frac{D_o}{D_i}\right)}{2\pi\lambda_p L}$ is the thermal resistance; λ_p is the thermal conductivity of the tube; D_o is

437   the outer tube diameter; and T_{po} is the outer surface temperature of the tube.

438   The 3D thermal conduction through the heating slab is given by:

439     $\Phi_{Cond} = \lambda_c F (T_{po} \text{-} T_{s,\infty}) = \frac{(T_{po} - T_{pi})}{R_{cond}}$ (13)

440   where $R_{cond} = \frac{1}{\lambda_c F}$ is the thermal resistance; λ_c is the thermal conductivity of the anhydrite

441   slab; and F is the shape factor which can be expressed as [31]:

442     $F = \frac{\pi L}{ln\left[\frac{2l}{\pi D_o} sh\left(\frac{2\pi e}{l}\right)\right]}$ (14)

443   where e is the thickness of heating slab; l is the distance between pipes; and L is the length in

444   the x-direction of the radiant slab.

445   The thermal convection and radiation between the heating slab surface and the ambient air

446   are given by:

447     $\Phi_{Conv\_a} = \frac{(T_{s,\infty} - T_a)}{R_{conv\_a}}$ (15)

448   And, assuming that $T_{surr} \approx T_a$, the radiative heat flux is:

449     $\Phi_{rad} = \frac{(T_{s,\infty} - T_{surr})}{R_{rad}}$ (16)

450 where $R_{conv\_a} = \frac{1}{h_{conv\_a}A_s}$ and $R_{rad} = \frac{1}{h_{rad}A_s}$ are the thermal resistances of the convective and

451 radiative heat transfer, respectively; T_a is the ambient air temperature; h_{conv_a} is the

452 convective heat transfer coefficient; and h_{rad} is the linearized radiative heat transfer

453 coefficients; T_{surr} is the surrounding temperature. The thermal resistances can be combined

454 into a single thermal resistance coefficient expressed by:

455 $R_a = \frac{R_{conv\_a}R_{rad}}{R_{conv\_a}+R_{rad}}$ (17)

456 The steady-state surface temperature $T_{s,\infty}$ of the floor heating system is then derived from the

457 overall energy balance equation as follows:

458 $T_{s,\infty} = \frac{(\overline{T_f}-T_a)}{R_a+R_{conv\_f}+R_p+R_{cond}}R_a + T_a$ (18)

459 As the heating slab is considered as a heat exchanger, the heat flux rate between the hot water

460 and the cold environment can be calculated using the logarithmic mean temperature

461 difference [28] as follows:

462 $\phi = U\frac{(T_{f,o}-T_{a,o})-(T_{f,i}-T_{a,i})}{ln(\frac{T_{f,o}-T_a}{T_{f,i}-T_a})} = \dot{m}_f C_{p,f}(T_{f,i}-T_{f,o})$ (19)

463 where $U = \frac{1}{\sum_n R_n}$ is the total heat transfer coefficient (from the hot water to the ambient air);

464 $T_{f,i}$ and $T_{f,o}$ are the inlet and the outlet hot water temperatures, respectively; $T_{a,i}$ and $T_{a,o}$ are

465 the ambient air temperatures at $x = 0$ and L, respectively, both assumed equal to T_a because

466 of the high air volume; $\dot{m}_f$ is the water mass flowrate; and $C_{p,f}$ is the water specific heat.

467
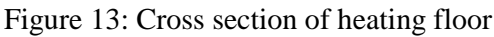
468 Figure 13: Cross section of heating floor

469

470 From Eq. 19 the outlet temperature of the hot water can be calculated:

471 $T_{f,o} = T_a + (T_{f,i} - T_a)e^{-\frac{US}{\dot{m}_f C_{p,f}}}$ (20)

472   The temperature T_x of the water at position x (Fig. 13) of the pipe is given by:

473    $$T_x = T_a + (T_{f,i} - T_a)e^{-\frac{U_x S_x}{\dot{m}_f C_{p,f}}} \tag{21}$$

474   where U_x and S_x are the overall heat transfer coefficient and heat exchange surface at

475   position x of the pipe.

476   As a final point, integration of T_x over the total length of the tube L yields the average

477   temperature of the hot water $\overline{T_f}$:

478    $$\overline{T_f} = \frac{1}{L}\int_0^L T_x \, dx = T_a + (T_{f,i} - T_a \left(\frac{1-e^{-\zeta}}{\zeta}\right)) \tag{22}$$

479   where $\zeta = \frac{US}{\dot{m}_f C_{p,f}}$.

5.2. Determination of τ and t_d using DoE method

481   Design of experiments is a systematic and rigorous approach to engineering problem-

482   solving that applies principles and techniques, at the data collection stage, so as to ensure the

483   generation of valid, defensible, and supportable engineering conclusions. The benefit of using

484   the DoE method is the provision of polynomial statistical meta-models with correlation

485   factors and factor interactions for all responses [32]. In the present case study, the response

486   factors are time constant τ and the delay time t_d, and the test will be conducted using the

487   validated 2D FDM numerical model. Numerous factors influencing τ and t_d need to be

488   considered: those related to the ambient air properties $\rho_a, \lambda_a, C_{p,a}$, and h_{conv_a}, h_r; the

489   anhydrite slab thermo-physical properties ρ , λ , C_p, and ε; the thermo-physical properties of

490   the hot water $\rho_f, \lambda_f, C_{p,f}, h_f$, and $\dot{V}$; and the geometric parameters e and D_i.

491   To simplify the process, a number of assumptions have been made. The ambient air

492   temperature was set to be $T_a = 16$ °C–28 °C. We assumed that ρ_a, λ_a, and $C_{p,a}$ remain

493   essentially constant in this temperature range and, as a result, the heat transfer coefficients

494   (h_{conv_a}, h_r, and h_{conv_f}) resulting from these parameters are kept constant. Similarly, the hot

495   water temperature was set between 27.5 °C–31.5 °C for the given experimental scenarios.

496   Therefore, the values of ρ_f, λ_f, and $C_{p,f}$, undergoing small changes in this range, are taken at

497   an average temperature of 30 °C. Table 4 presents the range variation of the remaining

498   parameters based on the recommendations of the French standard union AFNOR [29] as

499   recognized by the Centre of Scientific and Technical Building Studies. For simplicity, and for

500   practical reasons, a label (from A to F) is assigned to each parameter.

501

502   Table 4: Variations of FHS factors influencing τ and t_d [29]

503

504   A full factorial plan was adopted to provide all the required data from the DoE. As a

505   result, $2^6 = 64$ simulations, including all interactions between the six parameters listed in

506   table 4, were performed. In addition, statistical data was obtained by implementing each

507   factor combination in the 2D model. The temperature profiles obtained from the 2D FDM

508   model were then post-treated using a nonlinear regression method to obtain numerical values

509   of τ and t_d. Once all the values of τ and t_d were obtained, the meta-models of τ and t_d were

510   generated. The reduced statistical meta-models of τ and t_d obtained by the full factorial DoE

511   for the factors in Table 4 and in the given ranges of variation, are expressed, respectively, as

512   follows:

513     $\tau = (22.16 - 98\,e - 1.34\,\lambda + 0.00006\,\rho + 0.0016\,Cp - 23.3\,\dot{V} + 1257\,Di +$

514         $0.37\,e\rho + 0.47\,eCp - 15465\,eDi + 0.000008\,\rho Cp - 0.76\,\rho Di - 1.02\,CpDi)^2$

515   (23)

516     $t_d = 1532 + 6586\,e + 342\,\lambda - 0.0745\,\rho - 0.0543\,Cp + 3109\,\dot{V} + 5390\,Di -$

517         $6936\,e\lambda + 5.14\,e\rho + 8.88\,eCp + 7533\,\lambda Di - 9.02\,CpDi - 366133\,\dot{V}Di$ (24)

518   Because of using the DoE method, the sensitivity analysis could highlight the effect of

519   each factor and their interactions on the time constant τ and the delay time t_d. The Pareto

520   charts shown in Figs. 14 and 15 exhibit the influence of the parameters on the responses with

521   a confidence level of 95%. It can be seen that the primary factors influencing the thermal

522   inertia of the FHS (i.e., τ and t_d) are the slab thickness, the thermal conductivity, the specific

523   heat, the material density, and the volume flowrate. In other words, the thermal diffusivity of

524   the slab material and the water flow velocity are the primary parameters that should be used to

525   optimize the thermal response of the FHS.

526

527

528   Figure 14: Pareto chart of normalized effects (α=0.05) for time constant τ

529

530   Figure 15: Pareto chart of normalized effects ($\alpha = 0.05$) for delay time t_d

531

532   The effect of each factor on τ and t_d can be quantified by the slope of its plot obtained by

533   changing the values of the factors while keeping the levels of the other factors constant (Fig.

534   16). The slope indicates the variation of the response. It is observed that τ increases when e,

535   ρ, and C_p increase, and decreases when λ and $\dot{V}$ increase, and vice versa. The influence of the

536   tube inner diameter d is not significant.

537

538

539   Figure 16: Primary effects for time constant τ

540

541

542   Figure 17 shows the influence of the different primary factors on the delay time t_d.

543   It is observed that t_d increases when e, ρ, and C_p increase, and decreases when λ and $\dot{V}$

544   increase, and vice versa. The influence of the tube inner diameter D_i on t_d is not significant.

545

546   Figure 17: Primary effects for delay time t_d

547

548

549

550   **5.3. Validation**

551   The input parameters obtained from these case studies were implemented in the meta-

552   models (Eqs. 23 and 24) to provide both the time constant τ and the delay time t_d.

553   Considering the shape of the experimental curve that expresses the time evolution of the

554   surface temperature of the slab, τ corresponds to the time required for the temperature profile

555   to reach $\left(1 - \frac{1}{e}\right) \sim 63\%$ of its value at the steady state. Once the surface temperature $T_{s,\infty}$ has

556   reached the steady state, the time constant τ and the delay time t_d are calculated using Eqs. 23

557   and 24, respectively. Their values are substituted into Eq. 9 to estimate the time-dependent

558   average surface temperature of the radiant slab. Table 5 compares the calculated τ and d t_d

559   with the experimental ones.

560

561   Table 5: Comparison between calculated and measured time constant and delay time

562

563   Figure 18 compares the semi-analytical model with the 2D FDM and the 3D FVM models

564   as well as with experimental data for the average surface temperature under steady- and

565   unsteady-state conditions. The semi-analytical model exhibits a relatively good agreement

566   with the experimental data, as the maximum error is 1.1 °C (4%). This deviation is primarily

567   related to the assumptions of the model, which consider a logarithmic profile for the surface

568   temperature. However, given the simplicity of the model, which represents a significant

569   advantage when looking for fast and reliable results, it can be considered as a useful tool for

570   the estimation and analysis of the thermal behavior of a radiant slab.

Figure 18: Average surface temperature obtained from simplified model. Comparison with

measurements and simulation results

6. Conclusions

This study devoted to the heating floor surface temperature in transient condition proposed an innovative simplified semi-analytical model using a logarithmic temporal profile with time constant and delay time as the primary functional parameters. The proposed model, which was experimentally validated, was able to model the thermal behavior of the FHS in the full-scale test room under transient conditions. The experimental tests were repeated three times for two different scenarios considering the inlet water temperature set points. The average surface temperature, the in-depth slab temperature, the outlet/inlet water temperature, the indoor temperature, and the heat flow rate were the primary parameters that were directly measured. Both the time constant and the delay time, were derived from the experimental data. The response factors of the simplified model, namely τ and t_d, were obtained by a DoE method and a validated 2D FDM. The numerical values of the delay and constant times were in close agreement with the experimental values. The FDM model yielded satisfactory results for this case study as the relative deviation on the average surface temperature and the in-depth temperatures were smaller than 2% and 3%, respectively. In addition, a sensitivity analysis was conducted to show the effects of the different factors on the time constant and the delay time. It was shown that thickness, thermal conductivity, specific heat, material density, and the water volume flowrates had a significant influence on the thermal inertia of the FHS (characterized by τ and t_d), whereas, the inner tube diameter had no influence. Using the developed correlations for the time constant and delay time, the semi-analytical

model was able to estimate the average surface temperature with a relative error of 4% compared to the experimental results.

From the obtained results, the developed simplified model will be beneficial as it provides a useful and accurate way for a fast estimation of the floor surface temperature, the total heat flux, as well as the thermal inertia parameters of the FHS under dynamic running conditions. In addition, the developed DoE/FDM methodology could be used for the optimization of the FHS response and to obtain the optimal physical and design parameters and, thereby, improve its efficiency. Therefore, the simplified model could be a powerful tool for practicing building engineers and designers.

Acknowledgements

References

[1] B.W. Olesen, Radiant floor heating in theory and practice, ASHRAE J. 44 (7) (2002)19–24.

[2] Z. Wang, M. Song, F. Wang, Z. Ma, Q. Lin, Experimental investigation and seasonal performance assessment of a frost-free ASHP system with radiant floor heating, Energ. Build. 179 (2018) 200–212.

[3] A.J. Werner-Juszczuk, Experimental and numerical investigation of lightweight floor heating with metallised polyethylene radiant sheet, Energ. Build. 177 (2018) 23–32.

[4] D. Zhang, N. Cai, Z. Wang, Experimental and numerical analysis of lightweight radiant floor heating system, Energ. Build. 61 (2013) 260–266.

[5] S. Thomas, P-Y. Franck, P. André, Model validation of a dynamic embedded water base surface heat emitting system for buildings, Build. Simul. 4 (2011) 41–48.

[6] A. Merabtine, S. Mokraoui, A. Kheiri, A. Darss, Experimental and multidimensional numerical analysis of the thermal behavior of an anhydrite radiant slab floor heating system: a multi-objective sensitivity study, Energ. Build. 174 (2018) 619–634.

[7] M. Shin, K. Rhee, S. Ryu, M. Yeo, K. Kim, Design of radiant floor heating panel in view of floor surface temperatures, Build. Environ. 92 (2015) 559–577.

[8] M. Tahersima, P. Tikalsky, Experimental and numerical study on heating performance of the mass and thin concrete radiant floors with ground source systems, Const. Build. Mat. 178 (2018) 360–371.

[9] European Standard EN 15316-1:2017, Energy Performance of Buildings. Method for Calculation of System Energy Requirements and System Efficiencies. General and Energy performance expression, Module M3-1, M3-4, M3-9, M8-1, Technical Report, CEN, Bruxelles, BE, 2017.

[10] A. Kollmar, W. Liese, Die strahlungsheizung, 4th Ed. Munchen. R. Oldenbourg, 1957.

[11] A.K. Athienitis, Theoretical Investigation of thermal performance of a passive solar building with floor radiant heating, Solar Energ. 61(5) (1997)337–345.

[12] I. Kilkis, S. Sager, M. Uludag, A simplified model for radiant heating and cooling panels, Simul. Pract. Theo. 2 (1994) 61–76.

[13] J. Ren, L. Zhu, Y. Wang, C. Wang, W. Xiong, Very low temperature radiant heating/cooling indoor end system for efficient use of renewable energies, Solar Energ. 84 (2010) 1072–1083.

[14] S.Y. Ho, R.E. Hayes, R.K. Wood, Simulation of the dynamic behavior of a hydronic floor heating system, Heat Recov. Syst. CHP 15(6) (1995) 505–519.

644 [15] S. Sattari, B. Farhanieh. A parametric study on radiant floor heating system performance, Renew. Energ. 31 (2006) 1617–1626.

646 [16] A. Laouadi, Development of a radiant heating and cooling model for building energy simulation software, Build. Environ. 39 (2004) 421–431.

648 [17] S. Larsen, C. Filippin, G. Lesino, Transient simulation of a storage floor with a heating/cooling parallel pipe system, Build. Simul.: Int. J. 3(2) (2010) 105–115.

650 [18] F. De Monte, Transient heat conduction in one-dimensional composite slab. A 'natural' analytic approach, Int. J. Heat Mass Transf. 43(19) (2000) 3607–3619.

652 [19] X. Lu, P. Tervola, Transient heat conduction in the composite slab-analytical method, J Physics A: Mathematical and General 38(1): 81.

654 [20] M. Koschenz, B. Lehmann, Thermoaktive Bauteilsysteme Tabs, EMPAEnergiesysteme/ Haustechnik, Zurikh, 2000 (in German).

656 [21] R. Holopainen, P. Tuomaala, J. Piipo, Uneven gridding of thermal nodal networks in floor heating simulations, Energ. Build. 39(10) (2007) 1107-1114.

658 [22] X. Jin, X. Zhang, Y. Luo, A calculation method for the floor surface temperature in radiant floor system, Energ. Build. 42 (2010) 1753–1758.

660 [23] L. Zhang, X-H. Liu, Y. Jiang, Simplified calculation for cooling/heating capacity, surface temperature distribution of radiant floor Energ. Build. 55 (2012) 397–404.

662 [24] Z. Tian, B. Duan, X. Niu, Q. Hu, J. Niu, Establishment and experimental validation of a dynamic heat transfer model for concrete radiant cooling slab based on reaction coefficient method, Energ. Build. 82 (2014) 330–340.

665 [25] Q-Q. Li, C. Chen, Y. Zhang, J. Lin, H-S Ling, Simplified thermal calculation method for floor structure in radiant floor cooling system, Energ. Build. 74 (2014) 182–190.

667   [26] X.Wu, J. Zhao, B.W. Olesen, L. Fang, F. Wang, A new simplified model to calculate

668   surface temperature and heat transfer of radiant floor heating and cooling systems,

669   Energ. Build. 105 (2015) 285–293.

670   [27] S.V. Patankar, Numerical heat transfer and fluid flow, Hemisphere Publishing

671   Corporation, McGraw Hill Book Company, New York. 1980.

672   [28] F.P. Incropera, D.P. Dewitt, T.L. Bergman, A.S. Lavine, Fundamentals of heat and mass

673   transfer, 6th Edition, John Wiley & Sons, 2007.

674   [29] Centre Scientifique et technique du Bâtiment (CSTB), Document Technique Unifié NF

675   DTU 26.2 P1-1, Chapes et dalles à base de liants hydrauliques: Cahier des clauses

676   techniques types. AFNOR, 2008

677   [30] P. Pierson et J. Padet, Etude théorique et expérimentale des échangeurs thermiques

678   instationnaires: Simulation d'une phase de relaxation, Int. J. Heat Mass Transfer 31

679   (1988), 1577–1586.

680   [31] J.P Holman, Heat Transfer, Mcgraw-Hill Series in Mechanical Engineering, 10th edition,

681   New York, 2009.

682   [32] N. Khanna, Design of experiments in titanium metal cutting research, Springer, 2016

683

684
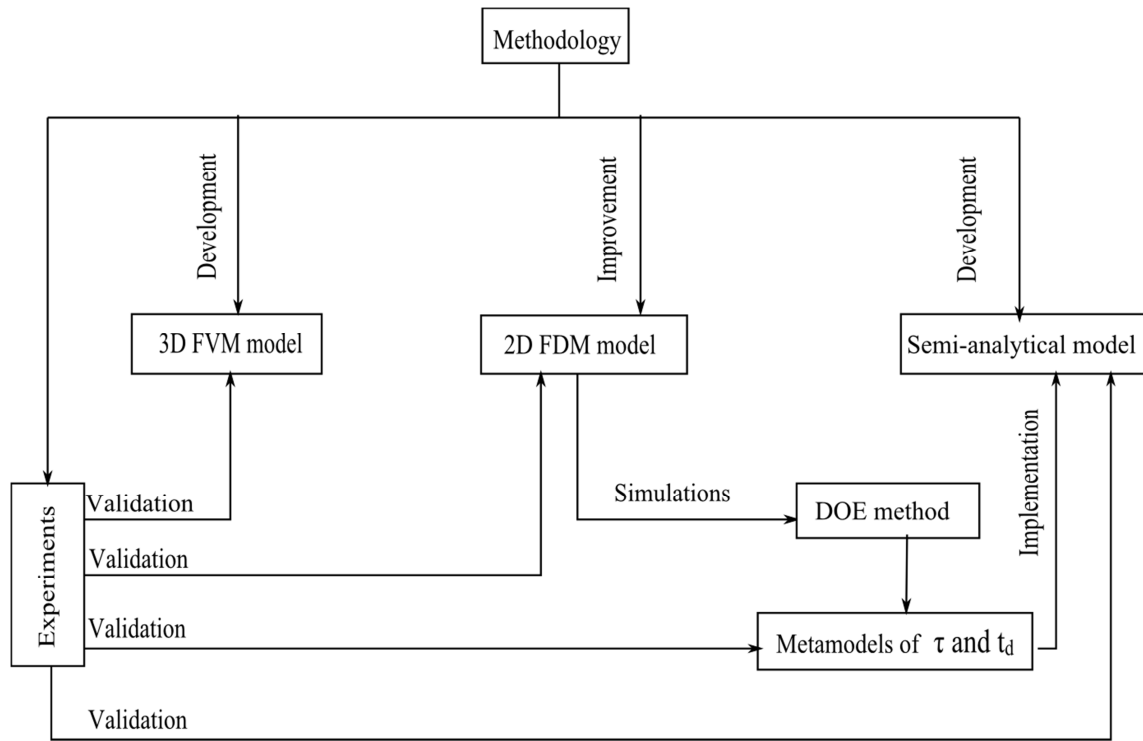
685

686   Figure 1: Schematic diagram of proposed methodology

687

688   (a)

① Wood fiber insulation
② Hemp wool insulation
③ 9mm thick wood board
④ outside wall
⑤ 100mm of air gap
⑥ Wood frame 45*120mm
⑦ Natural douglas cladding
⑧ 25mm of air gap
⑨ RH and temperature sensor
⑩ Average radiant temperature sensor
⑪ Surface temperature sensor
⑫ Fluxmeter
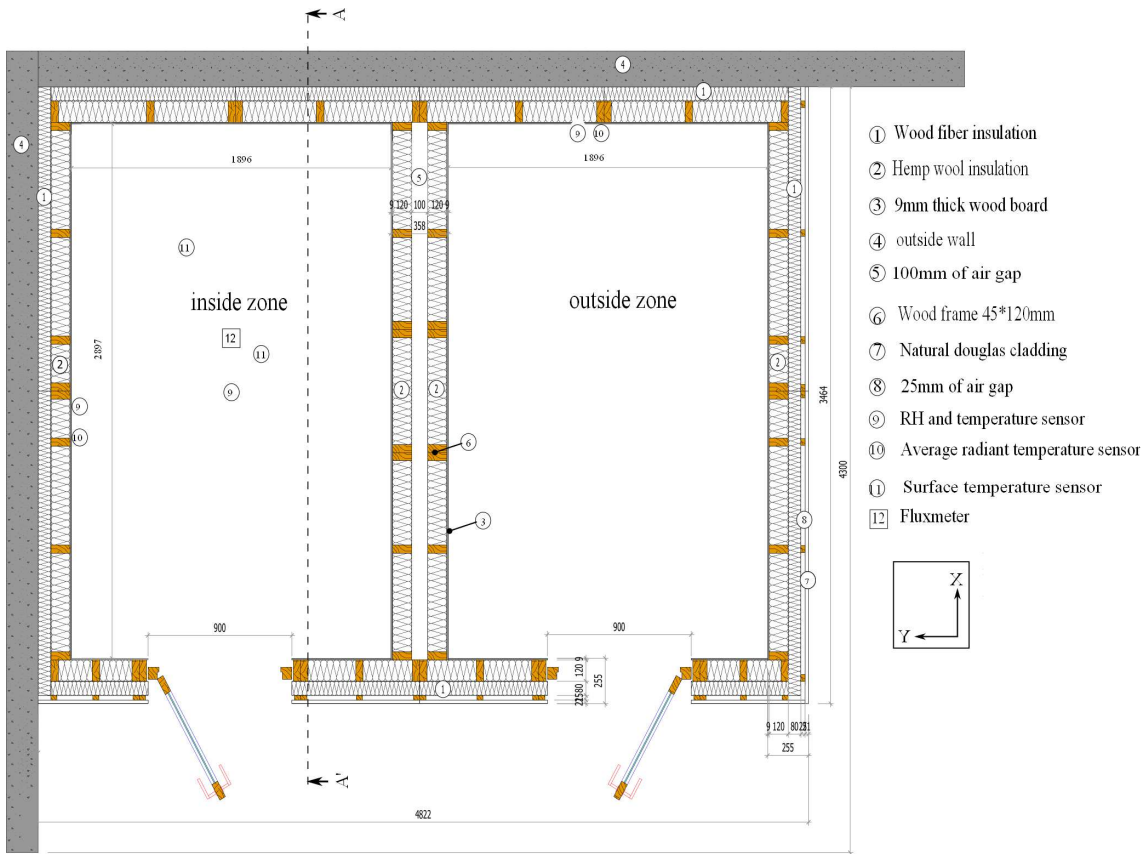
689

690   (b)

691   Figure 2: Experimental test cell: (a) outside view, and (b) plane view

1 Heat pump
2 Buffer tank
3 Water pumps
4 VAV
5 Radiators
6 Radiant slab
7 Cooler
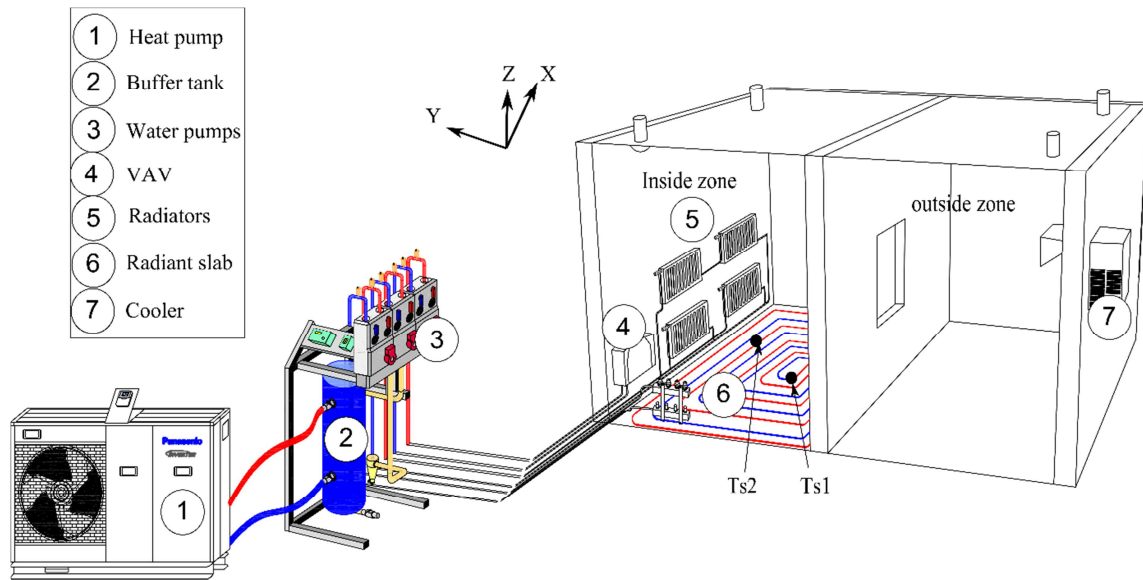
692

693   Figure 3: HVAC systems

694 Table 1: Test cell facility overview

Designation, devices and scenarios	Characteristics
Insulation materials	**Hemp wool** $\rho = 25$ kgm^{-3} ; $\lambda = 0.04$ W$m^{-1}K^{-1}$ **Wood fibers** $\rho = 40$ kgm^{-3} ; $\lambda = 0.04$ W$m^{-1}K^{-1}$
HVAC systems	**Air ventilation system** consisting on a dual-flow ventilation equipped with enthalpy wheels **Air conditioning system** is set to maintain the cold room at a temperature between -18 °C and 25 °C **Heating system** consisting of a VAV, four radiators and a FHS. The last consists of a tube coil placed on a wood fibers insulation panel and covered with an **anhydrite screed**. • **Anhydrite screed:** $e = 50\ mm$; $\rho = 1900$ kgm^{-3} ; $\lambda = 1.2$ W$m^{-1}K^{-1}$; $C_p = 1000$ J$kg^{-1}K^{-1}$; $\varepsilon = 0.94$; $S_{FHS} = 5.5\ m^2$; $floor\ to\ ceiling = 2.1\ m$ • **Insulation panel:** $e = 60\ mm$; $\rho = 40$ kgm^{-3} ; $\lambda = 0.04$ W$m^{-1}K^{-1}$; $C_p = 2100$ J$kg^{-1}K^{-1}$ • **Tube** coil is a cross-linked polyethylene tube $D_e = 16\ mm$; $D_i = 13\ mm$; $L = 51\ m$; $\rho = 933$ kgm^{-3} ; $\lambda = 0.4$ W$m^{-1}K^{-1}$; $\dot{V} = 0.02$ ls^{-1} ; The distance between pipes varies between 0.1 m and 0.15 m
Regulation system	The regulation system controls the inlet water temperature supplied in the FHS. This regulation is done by controlling a three-way valve that mixes both of the storage tank water and the return water from the heating floor.
Experimental scenarios	**Scenario #1**: the inlet water temperature follows two different steps, 27.5 °C ± 1°C between 0 and 600 min and 29 °C ± 1°C between 1700 and 2330 min. **Scenario #2**: the inlet water temperature is kept at a constant temperature of 31.5 °C± 1°C.

695

696 Table 2: Measuring instruments

Instrument	Amount	measured parameter	Measuring range	Accuracy	Image
Air RH and temperature sensor (KLU 100)	1	outdoor RH and temperature	[0, 100] % [-50, 50] °C	±2 % at 25°C ±0.5 °C at 0°C	
Air RH and temperature sensor (KLH 100)	1	indoor RH and temperature	[0, 100] % [-50, 50] °C	±2 % at 25°C ±0.5 °C at 25°C	

|					
Surface RH and temperature sensor (KLK 100)	1	Indoor RH and temperature	[0, 100] % [-50, 50] °C	±3 % at 25°C ±0.5 °C at 25°C	
Globe temperature sensor (ASTF-PT1000)	1	mean radiant temperature	[-30, 75] °C	±0.5 °C at 25°C	
Surface Temperature sensor (TEPK PT1000)	2	surface temperature of the inlet and the outlet water pipe	[-20, 80] °C	±0.3 °C at 0°C	
Temperature sensor (PT 1000)	2	surface temperature of the slab	[-20, 100] °C	±0.3 °C at 0°C	
Temperature sensor (PT 1000)	2	depth temperature of the slab	[-20, 100] °C	±0.3 ° C at 0°C	
Infrared thermal camera (FLUKE TR105)	1	infrared thermal imaging	[-20, 150] °C	±0.1 °C at 30°C	
Flux meter (AHLBORN FQA019C)	2	surface heat flux	[-260, 260] mV corresponding to <120 °C	±0.01 mV corresponding to ±0.12 °C	

697

698
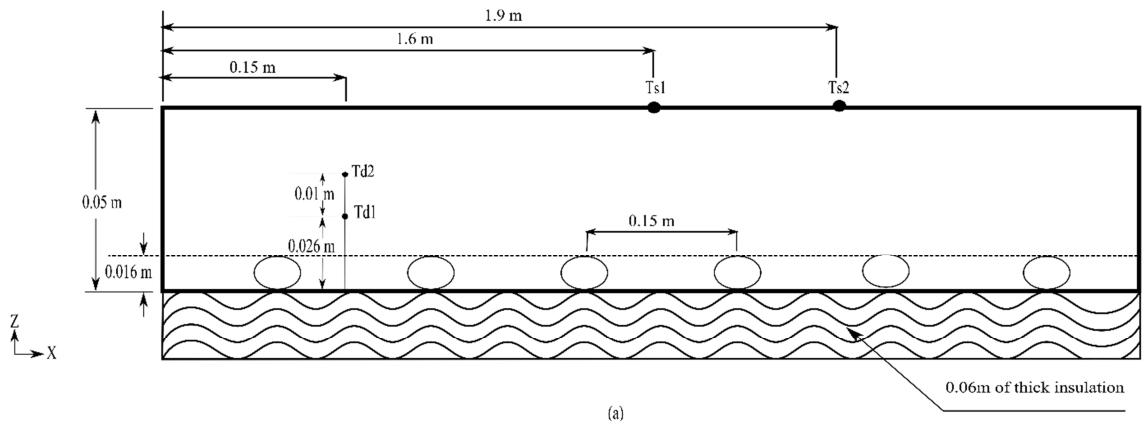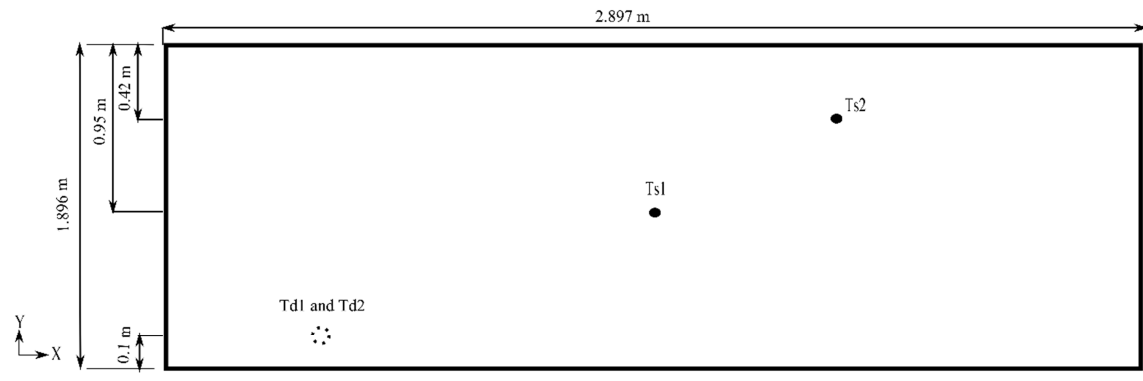
Figure 4: Sensor locations and slab dimensions: (a) cross-sectional view, and (b) top view
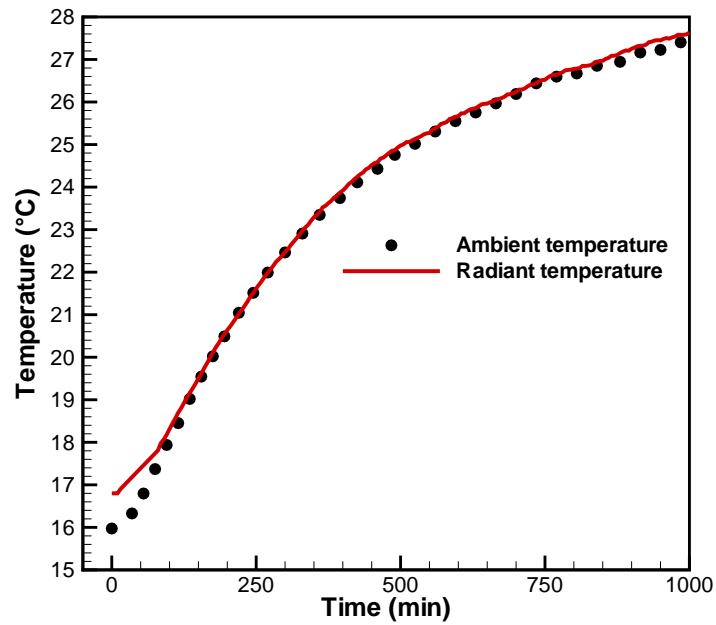
703   Figure 5: Air ambient and radiant temperature profiles in inside zone

704   Table 3: Comparison between three mesh levels

Mesh number	Nodes number	Average surface temperature (°C)	CPU time (hours)
#1	1 756 742	28.28	24
#2	2 144 428	28.94	36
#3	3 856 820	29.02	50

705

706
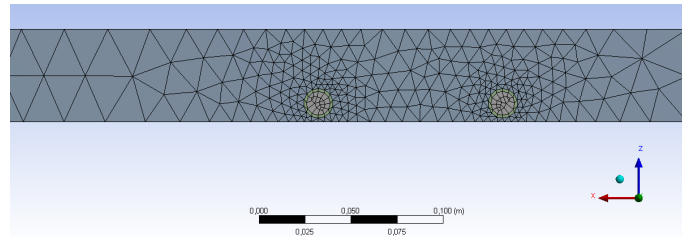
707
708   Figure 6: Domain meshing

709
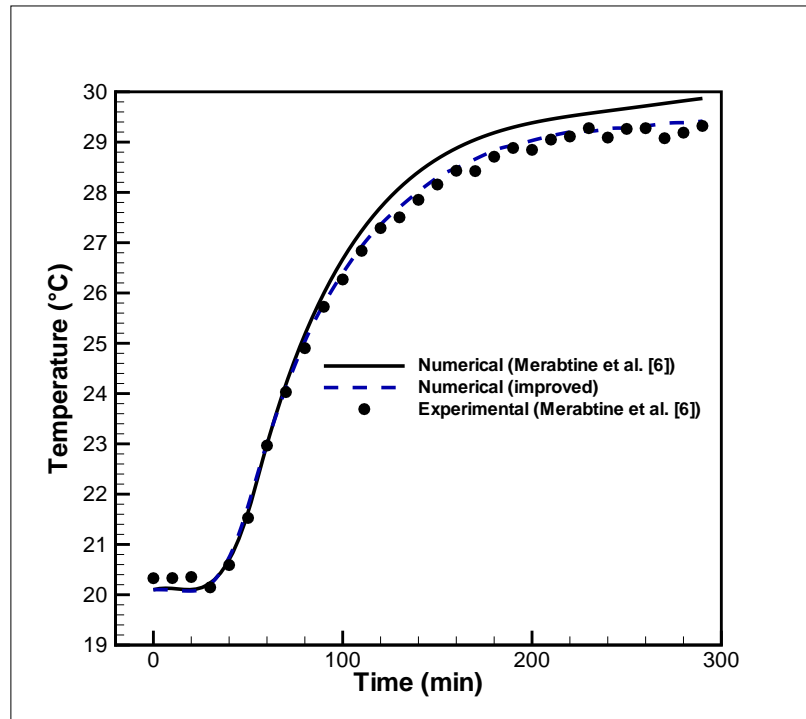
710

711   Figure 7: Average surface temperature profile (comparison with Merabtine et al. [6])

712

713
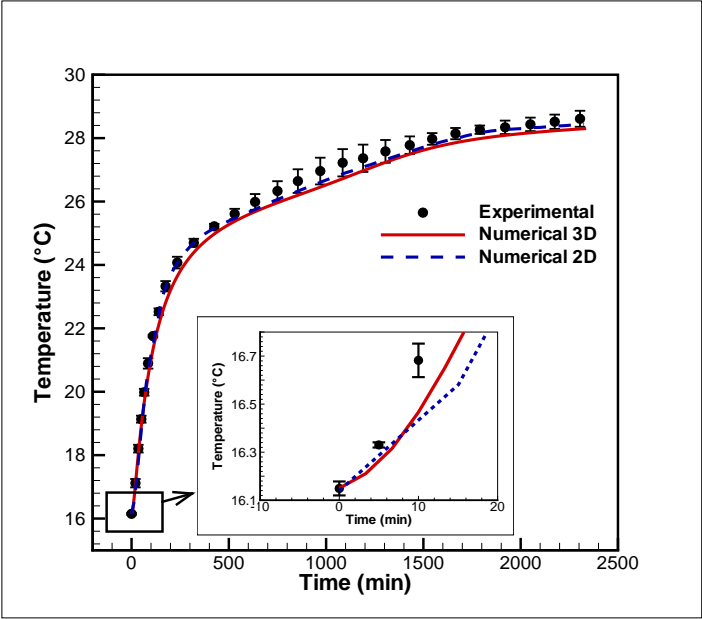
Figure 8: Average surface temperature profiles for scenario #1
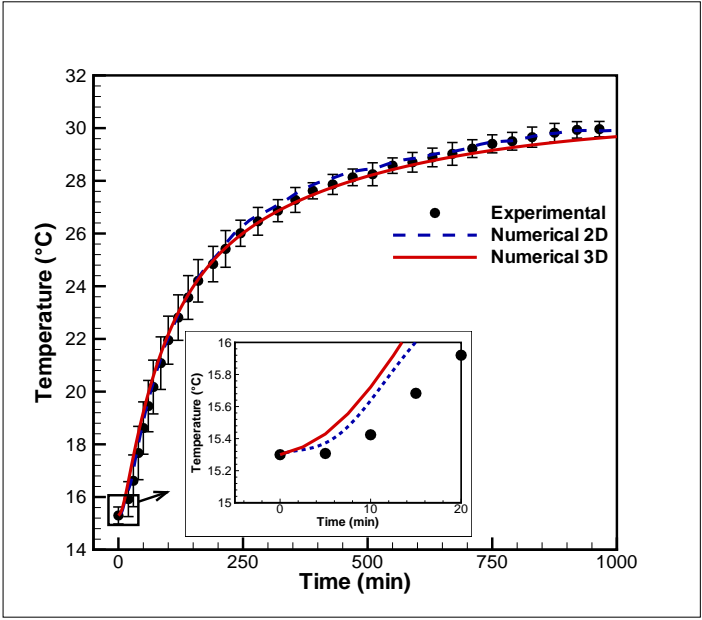
715

716

Figure 9: Average surface temperature profile for scenario #2
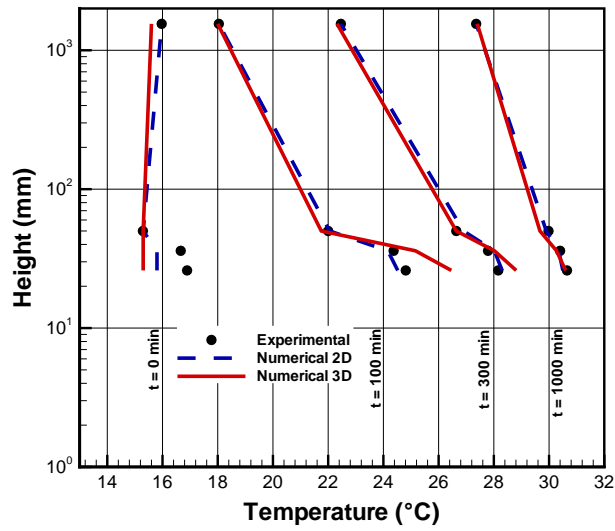
717

718   Figure 10: Floor heating temperature gradient from water pipes to ceiling for scenario #2

719
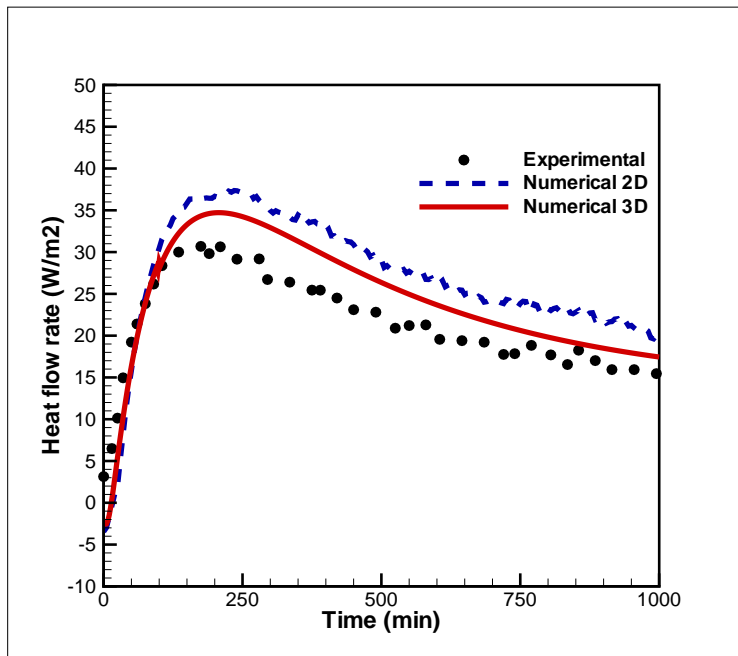
720

721   Figure 11: Average heat flow rate profile for scenario #2

722

723
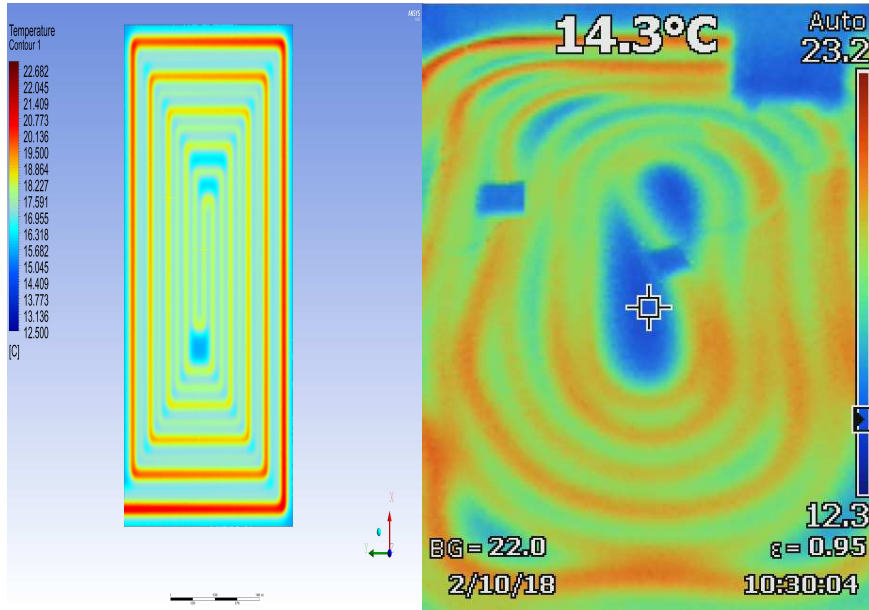
724

725
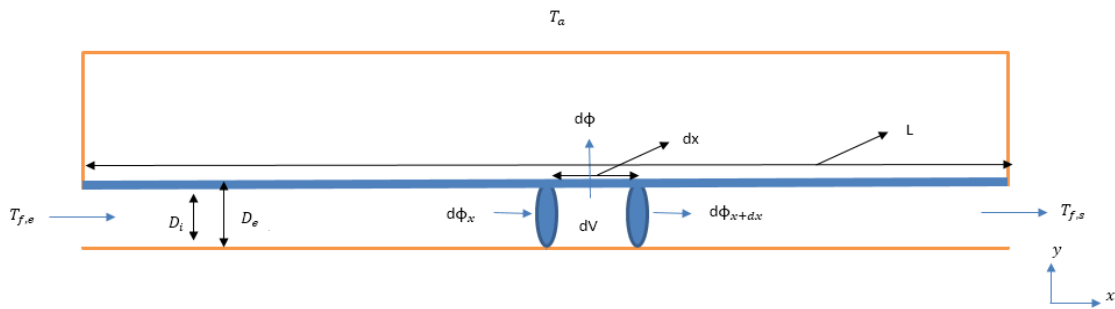
726   (a)   (b)

727   Figure 12: Surface temperature distribution at t = 30 min for scenario #2 (same temperature

728   scale): (a) numerical simulation, and (b) infrared thermal imaging

729

730

731

732   Figure 13: Cross section of heating floor

733   Table 4: Variations of FHS factors influencing τ and t_d [29]

Factors influencing τ and t_d	Labels	Levels	
		min (-1)	max (+1)
Slab thickness, e (m)	A	0.04	0.06
Thermal conductivity of the slab, λ (W.m-1.K-1)	B	1.2	2.6

Slab density, ρ (kgm-3)	C	1500	2500
Specific heat of the slab, C_p (J.kg-1.K-1)	D	1000	2000
Volume flow rate, $\dot{V}$ (L.s-1)	E	0.02	0.06
Tube inner diameter, D_i (m)	F	0.012	0.02

734
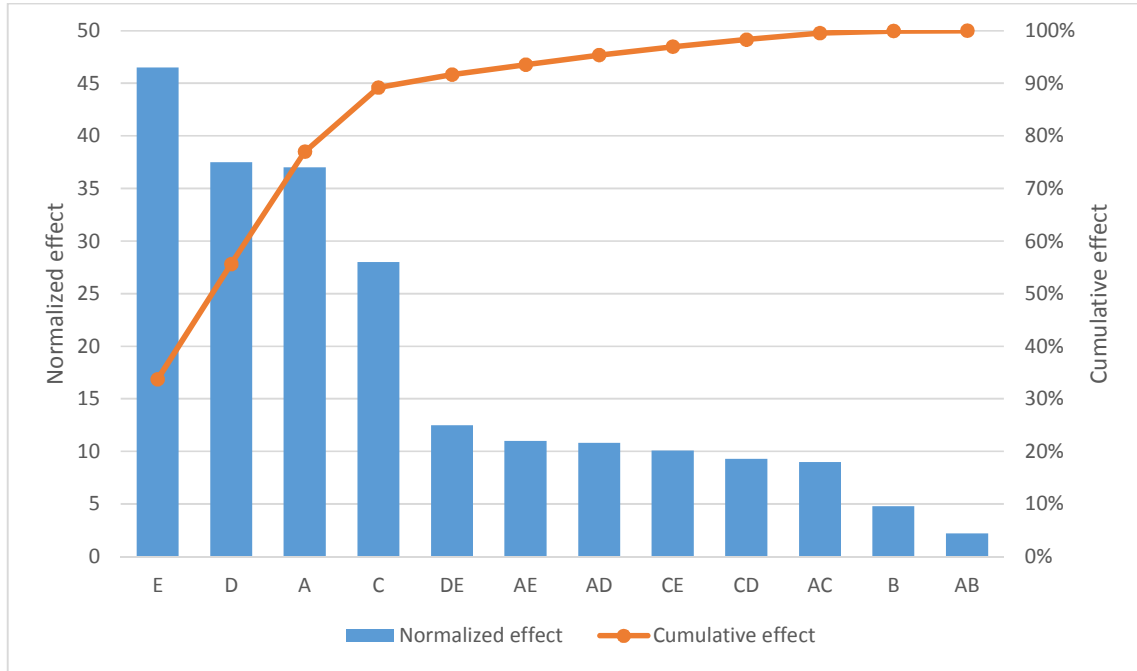
735

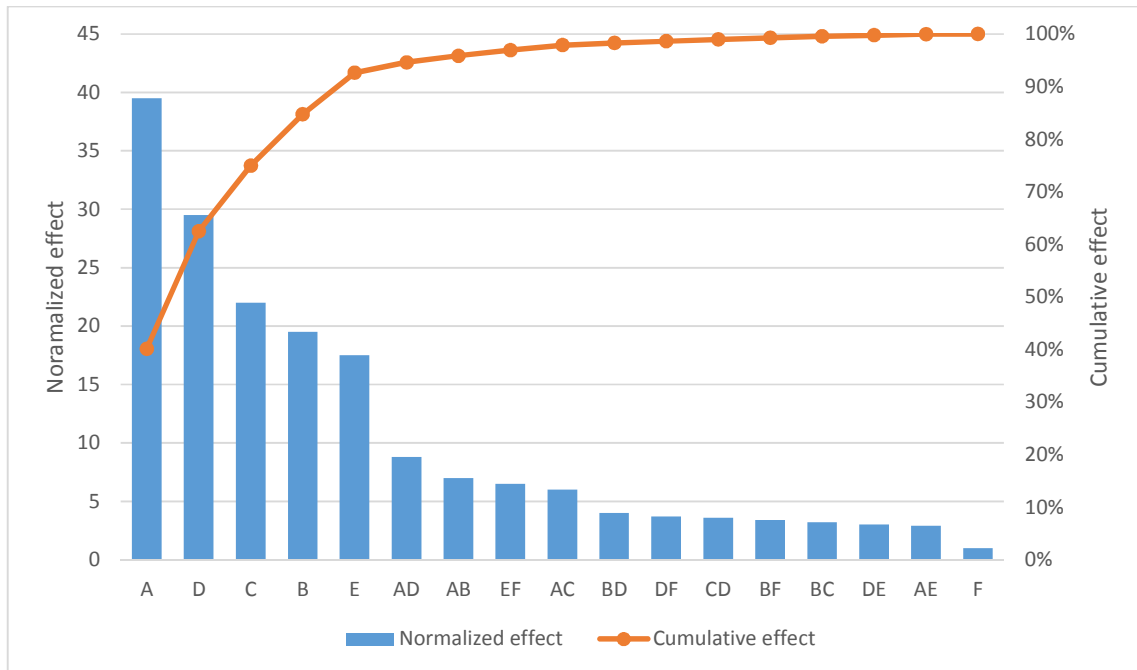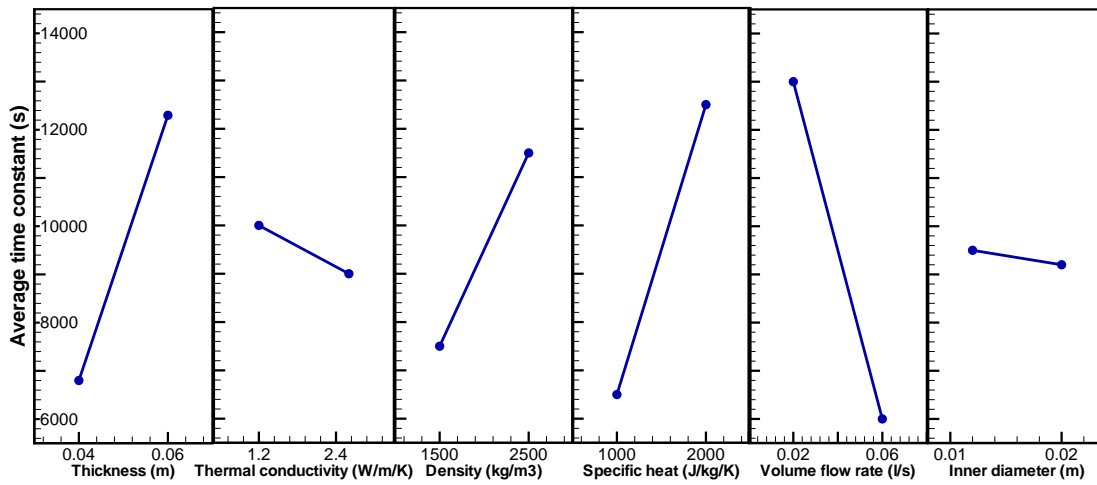736   Figure 14: Pareto chart of normalized effects (α=0.05) for time constant τ
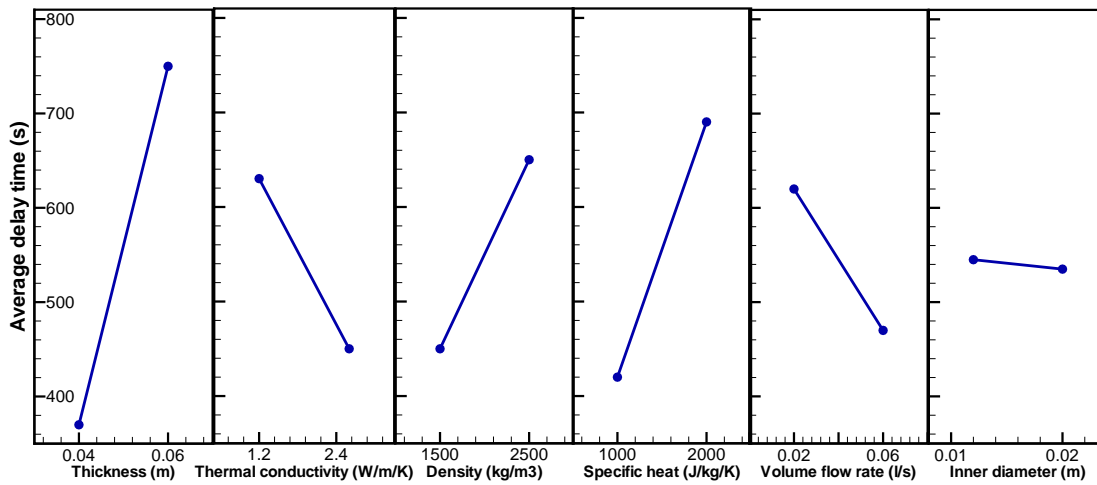
737

738

739   Figure 15: Pareto chart of normalized effects ($\alpha = 0.05$) for delay time t_d

740

741   Figure 16: Primary effects for time constant τ

742

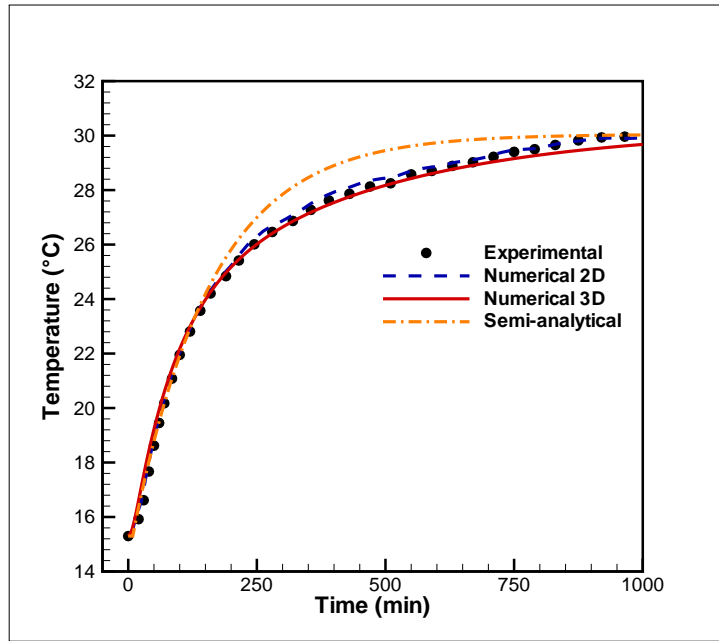743   Figure 17: Primary effects for delay time t_d

744

745   Table 5: Comparison between calculated and measured time constant and delay time

Parameter	Measurements (s)	Meta-model (s)	Relative deviation (%)
Time constant τ	9353	9188	1.76 %
Delay time t_d	503	527	4.77 %

Figure 18: Average surface temperature profiles for scenario #2

746

747

748